



## The bowtie-shaped deformation isotherm of superhydrophobic cylindrical mesopores

Loïc Michel, Lukas Ludescher, Viviana Cristiglio, Elisabeth Charlaix, Oskar Paris, Cyril Picard

### ► To cite this version:

Loïc Michel, Lukas Ludescher, Viviana Cristiglio, Elisabeth Charlaix, Oskar Paris, et al.. The bowtie-shaped deformation isotherm of superhydrophobic cylindrical mesopores. *Langmuir*, 2022, 38 (1), pp.211-220. 10.1021/acs.langmuir.1c02427 . hal-03630263

HAL Id: hal-03630263

<https://hal.science/hal-03630263>

Submitted on 4 Apr 2022

**HAL** is a multi-disciplinary open access archive for the deposit and dissemination of scientific research documents, whether they are published or not. The documents may come from teaching and research institutions in France or abroad, or from public or private research centers.

L'archive ouverte pluridisciplinaire **HAL**, est destinée au dépôt et à la diffusion de documents scientifiques de niveau recherche, publiés ou non, émanant des établissements d'enseignement et de recherche français ou étrangers, des laboratoires publics ou privés.

# The bowtie-shaped deformation isotherm of superhydrophobic cylindrical mesopores

Loïc Michel,<sup>†</sup> Lukas Ludescher,<sup>‡</sup> Viviana Cristiglio,<sup>¶</sup> Elisabeth Charlaix,<sup>†</sup> Oskar Paris,<sup>‡</sup> and Cyril Picard<sup>\*,†</sup>

<sup>†</sup>*Univ. Grenoble Alpes, CNRS, LIPhy, 38000 Grenoble, France*

<sup>‡</sup>*Institute of Physics, Montanuniversitaet Leoben, Franz-Josef-Strasse 18, 8700 Leoben, Austria*

<sup>¶</sup>*Institut Laue Langevin, 38042 Grenoble, France*

E-mail: [cyril.picard@univ-grenoble-alpes.fr](mailto:cyril.picard@univ-grenoble-alpes.fr)

## Abstract

Deformation of superhydrophobic cylindrical mesopores is studied during a cycle of forced water filling and spontaneous drying by *in situ* small-angle neutron scattering. A high pressure set up is put forward to characterize the deformation of ordered mesoporous silanized silica up to 80 MPa. Strain isotherms of individual pores are deduced from the shift of the Bragg spectrum associated to the deformation of the hexagonal pore lattice. Due to their superhydrophobic nature, pore walls do not cover with a pre-wetting film. This peculiarity gives the ability to use a simple mechanical model to describe both filled and empty pore state without the pitfall of disjoining pressure effects. By fitting our experimental data with this model we measured both the Young's modulus and the Poisson ratio of the nanometric silica wall. The measurement of this later parameter constitutes a specificity offered by superhydrophobic nanopores with respect to hydrophilic ones.

## 1 Introduction

Poromechanics or the study of the mechanical behaviour of porous material according to their fluid content is linked to various scientific fields such as acoustics, geophysics or biology<sup>1</sup>. A diversity of fluid/matrix couples have been studied<sup>2–4</sup>, with most of the works in this field dedicated to wetting or lyophilic situations. In particular during the past ten years a growing community has focused on the mechanics of various mesoporous silica and silicon when adsorbing fluids. Original results have been obtained concerning matrix deformation induced by fluid adsorption and pre-wetting film formation on solid walls and by inner liquid pressurisation subsequent to capillary condensation<sup>5–9</sup>. These results have been obtained specifically in lyophilic situations. For such systems the bulk fluid surrounding the mesoporous material is in a vapor state whereas the fluid within the pores can be in a liquid state due to its affinity for the considered solid. Elastic stresses within the solid matrix balance the pressure of the liquid within the pores as well as capillary forces coupled with disjoining pressure effects. The pressure of the bulk vapor surrounding the pores is used as a thermodynamic lever to control the state of the inner fluid but, because of its low value, it has very little direct mechanical impact

on the matrix deformation. When following an adsorption isotherm, a hysteretic deformation is observed with discontinuities on the adsorption and desorption branches associated to capillary condensation and drying<sup>6</sup>. This general behavior, observed in wetting or lyophilic situations, is however only one side of the story as recently illustrated with the measurement of a negative compressibility by forced liquid intrusion into the superhydrophobic nanoporous ZIF-8 material<sup>10,11</sup>. In the spirit of this work and of previous works dedicated to structural transition either induced from adsorption within pores or from external compression<sup>12</sup> this article aims at making the bridge between strain isotherms either built from an adsorption/desorption cycle or from an intrusion/extrusion cycle.

For this purpose we consider superhydrophobic mesopores combined with water. For such lyophobic systems the forced wetting and spontaneous drying of the mesopores occurs at large pressures of several tens of MPa. The bulk liquid surrounding the pores plays now an essential mechanical role. Such systems, put forward by Eroshenko as a way to store and retrieve mechanical energy<sup>13–15</sup>, have become the topic of an active field of fundamental research<sup>16–19</sup>. This trend strengthens the need of poromechanics studies of lyophobic systems in particular as the flexibility of matrices might have an impact on energy storage and recovery. Our goal here is to study the *in-situ* deformation of model superhydrophobic mesopores according to the chemical potential of the fluid this time fixed by the pressure of the bulk liquid surrounding the material.

Cylindrical ordered pores constitute a model geometry conducive to the experimental characterization of deformations as well as their theoretical modeling, as already demonstrated in the wetting case<sup>20–23</sup>. To investigate such systems in the non-wetting case, we consider hydrophobized micelle-templated silica structured as parallel monodisperse cylindrical mesopores arranged in a 2D hexagonal lattice. Unlike the wetting case for which the control of the pore content by means of the bulk vapor pressure is mostly based on vacuum technologies, the non-wetting case requires high pressure technologies, in liquid phase, compatible with volume changes to accommodate intrusion and extrusion processes<sup>24</sup>. The high pressure set up required for these experiments prevents the usage of a macroscopic approach such as dilatometry<sup>23,25</sup> to measure the deformation of the porous

matrix but fortunately local in-situ techniques reveals applicable for this purpose<sup>26,27</sup>. Small angle scattering techniques give the ability to extract radial deformation of cylindrical mesopores from a shift of their diffraction pattern<sup>5,6</sup>. To avoid the pitfall of contrast changes observed with X-ray scattering according to the filling level of the mesopores, we chose here to use small-angle neutron scattering (SANS) taking benefit of zero scattering length density of the fluid<sup>9</sup>. A specific high-pressure intrusiometer adapted for neutron scattering experiments has been designed to cover a pressure range up to 100 MPa in order to characterize the deformation of the pores along a full water intrusion/extrusion cycle. A hysteretic mechanical behavior is observed with discontinuities associated to liquid intrusion into the pores and extrusion out of the pores. Finally, mechanical properties of pores walls extracted from these measurements by means of an adequate mechanical model are compared to the properties measured in the wetting case for the same material. The absence of pre-wetting film formation in the non-wetting case reduces the number of parameters required for the theoretical analysis. This gives the ability to identify both the Young's modulus and the Poisson ratio of the nanometric-thin silica wall, which is not possible in the wetting case.

## 2 Material and method

### 2.1 Ultra-hydrophobic micelle templated silica

Ultra-hydrophobic micelle-templated silica MCM-41 are prepared following the protocol of Lefevre et al<sup>28</sup>. The preparation is divided into two steps, first the synthesis of siliceous hydrophilic particles, then the grafting of the silica surface to get superhydrophobic mesopores. Particles consist of a hexagonal lattice of cylindrical mesopores (see Figure 1) obtained from the condensation of silicates around a template made of hexadecyltrimethylammonium bromide (CTAB) cylindrical micelles. The crystalline structure of the

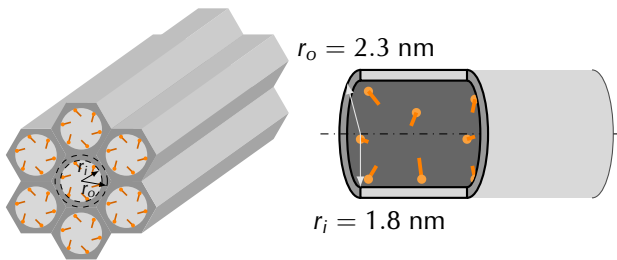


Figure 1: MCM-41 grafted with hydrophobic octyldimethylchlorosilane. The matrix is considered as the combination of individual silica nanotubes of inner radius  $r_i$  and outer radius  $r_o$ . The effective radius seen by the confined fluid taking into account the grafted muffle (either liquid or vapor) is  $r_g < r_i$ .

material is confirmed by X-ray powder diffraction (Malvern Panalytical X'Pert PRO MPD, see Figure 2A). The scattering vector length  $q_0 = 1.58 \text{ nm}^{-1}$  corresponds to the main Bragg

peak associated to the 100 reticular plane of the X-ray spectrum. This defines half the distance between the centers of two adjacent pores  $r_0 = 2\pi q_0^{-1}/\sqrt{3} = 2.3 \pm 0.01 \text{ nm}$ . The inner radius of the pore  $r_i = 1.8 \pm 0.05 \text{ nm}$  was determined from the nitrogen adsorption isotherm (Micromeritics ASAP 2020) by fitting experimental points with a model based on a Derjaguin-Broekhoff-de Boer approach<sup>19,29-31</sup> (see Supporting Information). The continuous red curve, in the inset of Figure 2A, is obtained with such a model considering a Gaussian pore-radius distribution the standard deviation of which is 13% of the mean pore radius. The hydrophilic pristine material is then silanized with *n*-octyl-dimethylchlorosilane to get superhydrophobic mesopores<sup>28</sup>. The non-wetting behaviour of the sample is characterized by mean of a home made intrusiometer<sup>19,32</sup>. The sample made of a suspension of grafted MCM-41 in water is placed into a dedicated deformable container immersed in glycerol as a pressure transmitting fluid within the measurement chamber of the apparatus. Experiments are carried out at fixed compression/dilation speed, by mean of a piston moving at constant velocity. The intrusion/extrusion cycle obtained with this apparatus is shown in Figure 2B, after subtraction of the elastic contribution due to liquid compressibility and system finite rigidity. This elastic contribution is characterized measuring the slope of the linear variation of the pressure with respect the volume before and after intrusion/extrusion processes<sup>24</sup>. Filling and emptying of mesopores are revealed by two plateaus characterized respectively by an average intrusion pressure  $p_{int} = 45 \text{ MPa}$  and an average extrusion pressure  $p_{ext} = 10 \text{ MPa}$ . The intrusion pressure distribution is well predicted (red dashed curve in Figure 2B) using the Laplace law of capillarity and the pore-size distribution extracted from nitrogen adsorption. The two average pressure levels  $p_{int}$  and  $p_{ext}$  are noticeably lower than the ones reported by Lefevre et al<sup>28</sup> for the same pristine material. These moderate pressure levels, compatible with the mechanical strength of the specific aluminium sample holder used for neutron scattering experiments, are related to the surface density in grafting agent. The molecular density of our sample, characterized by thermo-gravimetric analysis (Mettler-Toledo, LF1100-XP1), is  $0.65 \text{ nm}^{-2}$  based on the native material surface which is half the value of  $1.3 \text{ nm}^{-2}$  reached by Lefevre et al<sup>28</sup>.

### 2.2 High pressure intrusometry during neutron diffraction experiments

The high pressure set up which has been developed is usable on any neutron beam line for the characterization of a dense slurry of superhydrophobic nanoporous particles in water (see Figure 3). Compared to classical high pressure equipment, such as diamond anvil dedicated to GPa pressure range and minute deformations, our set-up works at pressures below 100 MPa and is able to accommodate large volume variations associated to water intrusion into the pores (or extrusion out of the pores). In addition, porous particles have to remained trapped within the measurement cell and should not move freely with the liquid when it is transported in and out of the nanopores, so that the total meso-

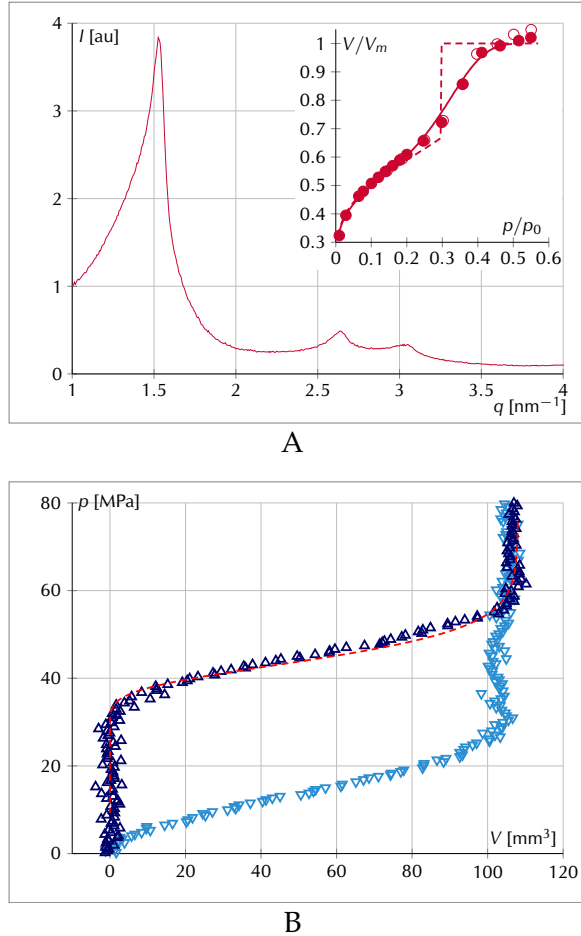


Figure 2: A) Powder X-ray diffraction spectrum of pristine silica. Inset: Adsorption (full symbols) and desorption (open symbols)  $N_2$  isotherms at 77 K with  $V_m = 510 \pm 10 \text{ mm}^3/\text{g}$  denoting the mesopores volume after condensation. The lines are fits of pre-wetting film up to capillary condensation for a single pore size (dashed line) or for a Gaussian pore radius distribution (full line). B) Corrected intrusion/extrusion isotherm of water in silanized MCM-41 (after subtracting the elastic deformation of the system) for 1 g of porous material at 20°C. The red dashed curve is the theoretical intrusion pressure distribution based on the Gaussian pore radius distribution obtained from  $N_2$  isotherms.

porous volume remains stable during the successive measurements. Moreover, compared to previous studies with hydrophilic particles surrounded with a vapor which did not contribute to the scattering signal, the superhydrophobic particles of interest are surrounded with a bulk liquid the density of which is closed to the confined liquid. This means that the bulk fluid may contribute to the signal. To limit as much as possible its contribution and favour the contribution of the powder we aim to reach a volume fraction in solid particles as high as possible. In addition, the thickness of the sample needs to be reduced as much as possible to avoid signal absorption and multiple scattering. Finally as

the state of the system is highly sensitive to the bulk liquid pressure and to the temperature, especially during the filling and emptying transitions, a stability of the pressure (with fluctuations smaller than  $\pm 0.5 \text{ MPa}$ ) and of the temperature (with fluctuations smaller than  $\pm 0.1 \text{ K}$  when working close to the ambient temperature) are needed. The central piece of the set-up is a cylindrical aluminium cell specially designed to minimize neutron absorption, with a total wall thickness of 2 mm and an internal diameter of 6 mm that can sustain 100 MPa. The cell hosts a cylindrical aluminium insert comprising a rectangular slit (1 mm thick, section  $6 \times 60 \text{ mm}^2$ ) used as a sample holder (see Supporting Information). The slit is filled with the dense wetted nanoporous powder, behaving as a paste, with a spatula. The dry friction within the granular media is large enough to maintain the sample in place within the slit during intrusion/extrusion phenomena. The cell is connected to a capillary tubing filled in water used to accommodate the volume of liquid moving in and out of the nanopores. The liquid pressurization is carried out by means of an automated syringe pump (VINCI) working with fluorinert FC-770 as a high pressure transmission media. A separator comprising a free sealed piston is used to prevent any mixing between the water and the oil and potential contamination of the porous matrix. A pressure sensor is mounted at the vicinity of the cell in order to check the experimental conditions. The cylindrical cell is finally placed within a home-made thermalization chamber, closed by thin aluminium foils. The lower and upper faces of the chamber are thermally regulated by a thermal bath. The temperature is homogenized within the chamber by forced air convection.

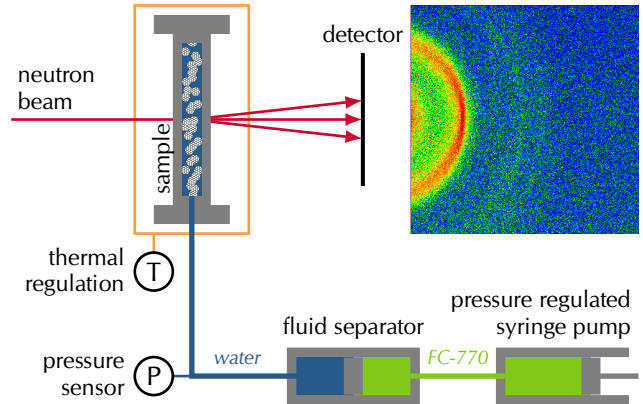


Figure 3: Schematic of the setup used for the study of the deformation of hydrophobized MCM-41 nanopores when performing an intrusion/extrusion isotherm. Inset: Typical 2D small-angle diffraction pattern obtained after calibration and instrument correction.

### 2.3 SANS experiments

Small angle neutron scattering experiments are carried out on the D16 ILL instrument. Neutrons offer the possibility to change the fluid scattering length density by isotope substitution. This helps one to prevent any unexpected alteration

of the diffraction pattern when changing the content of the pores<sup>33</sup>. For this purpose, water is prepared as a mixture of D<sub>2</sub>O and H<sub>2</sub>O to obtain an effective zero scattering length density. The D16 instrument at ILL is well suited for high resolution diffraction study for intermediate  $q$  range from 0.4 to 4.5 nm<sup>-1</sup> that contains all of our three Bragg peaks at 1.5, 2.6 and 3 nm<sup>-1</sup>. The percent resolution on wavelength and the small pixel size keeps peaks sharp and provide a fine  $q$  spacing of 0.02 nm<sup>-1</sup>. Acquisitions are carried out for a series of imposed pressures along an intrusion/extrusion cycle. Due to the moderate neutron flux of the D16 line at least 2 h are required for the acquisition of a single spectrum during which the pressure and the temperature are maintained stable enough to prevent any drift of the sample state. The detector is shifted from the center of the beam first to avoid the impact of the direct beam and second to reach large scattering vector needed to determine precisely the incoherent background. Calibration and corrections are carried out using three additional acquisitions. The background noise is obtained from an acquisition with a fully absorbing cadmium sample and then with an empty cell. The efficiency of each pixel of the detector is defined from an acquisition of a perfectly incoherent signal delivered by a pure water sample. The inset in Figure 3 shows a typical axisymmetrical 2D diffraction pattern obtained after calibration which leads to a typical spectrum after azimuthal integration as shown in Figure 4A).

For each measurement, the transmission, calculated as the ratio of the signal intensity with and without the sample in place, revealed to be a useful complementary quantity for this study. The transmission of the order of 64% decreases slightly when the water amount increases within the cell. In particular, we observed a relative decrease of the transmission of the order of 2% when water fills in the mesoporous particles. Following the transmission it was thus possible to confirm the empty or filled state of the pores according to the considered pressure. This relative change of the transmission is in line with the estimated ratio of the intruded volume over the external water volume between porous particle based on the amount of powder placed within the slit.

### 3 Results and discussion

#### 3.1 Strain during an intrusion/extrusion cycle

Each raw spectrum shows a clear main Bragg peak (reticular index 100) which characterizes the inter-pore distance of the hexagonal pore lattice. A small second peak is also visible which may correspond to the combined contribution of 110 and 200 peaks. In addition to the Bragg peaks of interest, the raw spectra present a base line visible at large  $q$  and a strong increase of the signal toward low  $q$ . These two contributions are not fully reproducible from one acquisition to another and need to be subtracted to be able to detect reliably any shift of the Bragg peak position. The careful correction of these two contributions is carried out with the following procedure. First, the base line measured at large  $q$  between 3.5 and 4.8 nm<sup>-1</sup> is suppressed. This corrected signal is characterized at low  $q$  by a power law decrease of its intensity (vis-

ible in the inset of Figure 4A after full correction) generally associated with Porod's law the exponent of which is related to the surface of the diffracting objects. In presence of well defined objects, with sharp interface, predictions of the exponent can be made. However in our case the size, the shape and the structure of the surface of the mesoporous particles is not the well defined. We thus identify the exponent from a regression in a log scale, to be able to estimate this Porod's contribution. After subtraction of this second correction, the base line is evaluated again taking into accounts the points for  $3.8 < q < 4.5$  nm<sup>-1</sup> and  $2.1 < q < 2.3$  nm<sup>-1</sup> between the two Bragg peaks. These admittedly arbitrary limits are chosen to base our correction on a maximal number of points while discarding points associated to Bragg peaks and points at large  $q$  subjected to large uncertainties. These limits are identical for the treatment of all spectra. For a given spectrum we checked that slight variations of these limits do not change noticeably our results. Figure 4A shows one typical raw spectrum. The gray curve represents the correction function of the form  $kq^{-n} + I_{\infty}$ , with  $I_{\infty}$  the intensity of the base line,  $n$  the pseudo Porod's exponent of the order of 1.6 in our case and  $k$  a prefactor. The two last parameters are, respectively, identified from the slope and the intercept of the linear fit in log scale.

After this correction, we finally normalized the intensity of the signal by the area of the main Bragg peak for  $q$  between  $q_{min} = 1$  nm<sup>-1</sup> and  $q_{max} = 2$  nm<sup>-1</sup>. This range has been chosen in order to consider most of the points which flanks the peak. As a result the corrected intensity  $I_c$  is in length unit and such that  $\int_{q_{min}}^{q_{max}} I_c(q) dq = 1$ . Figure 4B, shows this corrected intensity  $I_c$  of two typical spectra, measured at ambient pressure and at 40 MPa

The so obtained spectra are almost identical except a slight shift related to the radial deformation of the mesopores when changing the pressure. The next step of the analysis aims at extracting this slight shift as a function of the applied pressure. Various functions are conventionally used to fit diffraction peaks. Such an approach is well suited to identify the position of a peak with a good resolution as long as the number of parameters required for the fitting remain limited<sup>34</sup>. In our particular case, the slight polydispersity of the pore size and the presence of the hydrophobic grafted muffle prevent the use of simple function to fit properly our data. Moreover it is not exactly the position of the peak, but rather its shift according to the applied pressure which is of interest to measure the deformation of the mesoporous matrix. More precisely the deformation  $\epsilon$  of the sample is defined by the relative change of  $r_0 = 2\pi q_0^{-1} / \sqrt{3}$  or relative change in inter-pore distance, which correspond precisely to the opposite of the relative variation of the scattering vector length. Rather than doing a curve fitting, a more suitable approach in our case, to avoid any loss of information, consists on working directly on the difference between two experimental spectra. For this purpose we use the barycenter of the area below each corrected Bragg peak, in the range  $1 < q < 2$  nm<sup>-1</sup>, as a definition of the scattering vector  $q_p$  of this peak measured at a

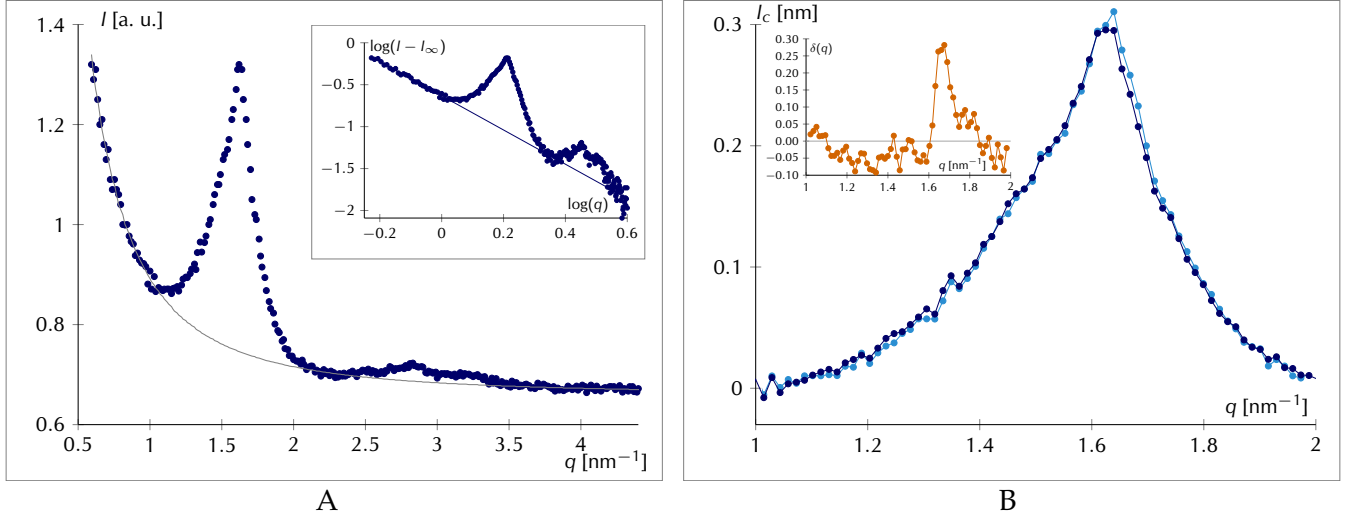


Figure 4: A) Raw diffraction spectrum for grafted MCM-41 obtained at ambient pressure. Gray curve: correction function taking into account Porod's contribution and base line (see text). Inset: logarithm of the corrected intensity  $I - I_\infty$  versus the logarithm of the scattering vector length  $q$  where  $I_\infty$  is the intensity of the base line. Lines are linear regression of experimental points. B) Comparison of the corrected intensity  $I_c$  between spectra at ambient pressure (dark blue) and 40 MPa (light blue) before pore filling. Inset: normalized difference  $\delta$ , as defined by eq. 3, between the  $q$  weighted intensities measured at 40 MPa and at ambient pressure.

given pressure  $p$ :

$$q_p = \int_{q_{min}}^{q_{max}} q I_c(q) dq \quad (1)$$

We checked here that the  $q_p$  value measured in such a way agrees with the value previously obtained from X-ray diffraction. From the dependence of  $q_p$  on pressure, our goal is to extract the relative variation of  $q_p$  with respect to a reference scattering vector  $q_{pr}$ , typically the scattering vector at ambient pressure.

$$\epsilon(p) = \frac{r_0(p) - r_0(p_r)}{r_0(p_r)} = -\frac{q_p - q_{pr}}{q_{pr}} = -\frac{1}{q_{pr}} \int_{q_{min}}^{q_{max}} \delta(q) dq \quad (2)$$

with  $\delta$  a function of  $q$  defined as the normalized difference between the two  $q$ -weighted spectra measured at pressures  $p_r$  and  $p$ :

$$\delta(q) = q(I_c(q) - I_{cr}(q)) \quad (3)$$

For a positive shift of the Bragg peak associated to the contraction of the porous matrix,  $\delta$  is negative on the ascending part of the peak and positive on its descending part (see inset of Figure 4B). Discrete integrals are calculated from experimental points using the trapezoidal rule. Our measurements are carried out at the limit of sensitivity of the technique. The uncertainty on our measurements, as suggested by the inset of Figure 4B, is important with respect to the shift in  $q$  we aim to measure. Varying the range of  $q$  values used for the correction of the spectrums and integrals calculation we estimated that the uncertainty is of the order of  $\pm 0.5 \times 10^{-3}$ . With such an uncertainty we are nevertheless able to extract slight deformation  $\epsilon$  associated to scattering vector shifts 10

times smaller than the experimental acquisition spacing in  $q$ .

The measured deformation  $\epsilon$  of our sample is shown in Figure 5A according to the applied pressure along an intrusion/extrusion cycle. This deformation presents a clear hysteretic behavior with a bow tie shape, which is qualitatively different from the one observed with hydrophilic MCM-41. Increasing the pressure (upward dark blue triangles) from ambient condition leads to a compression of the matrix which is revealed by a decrease of  $\epsilon$  down to a value of the order of  $-3 \times 10^{-3}$  at 40 MPa. Then a sudden relaxation is observed, the matrix is less compressed at 50 MPa than at 40 MPa. This matrix relaxation upon pressure increase can be seen as an effective auxetic behavior as recently put forward with ZIF-8 metal organic framework by Grosu et al<sup>10</sup>. Then, increasing further the pressure, up to 80 MPa, the compression continues again with a much less pronounced slope than before the relaxation step. Decreasing the pressure from this point (downward light blue triangles), we stick on this second behavior and observe a modest increase of  $\epsilon$  down to 10 MPa. A second jump occurs as the last point measured at ambient pressure is close to 0 corresponding to the initial reference value. The two jumps of  $\epsilon$ , first measured between 40 MPa and 50 MPa when the pressure increases and then below 10 MPa when the pressure decreases, coincide respectively with intrusion and extrusion processes further revealed by the pressure dependence of the transmission (see Figure 5B). When the pressure increases, the transmission slightly decreases in agreement with the water excess within the measurement cell associated to its compressibility. The transmission shows a marked decrease around 45 MPa. Then the transmission follows a pressure dependance with a similar slope as previously observed. When de-

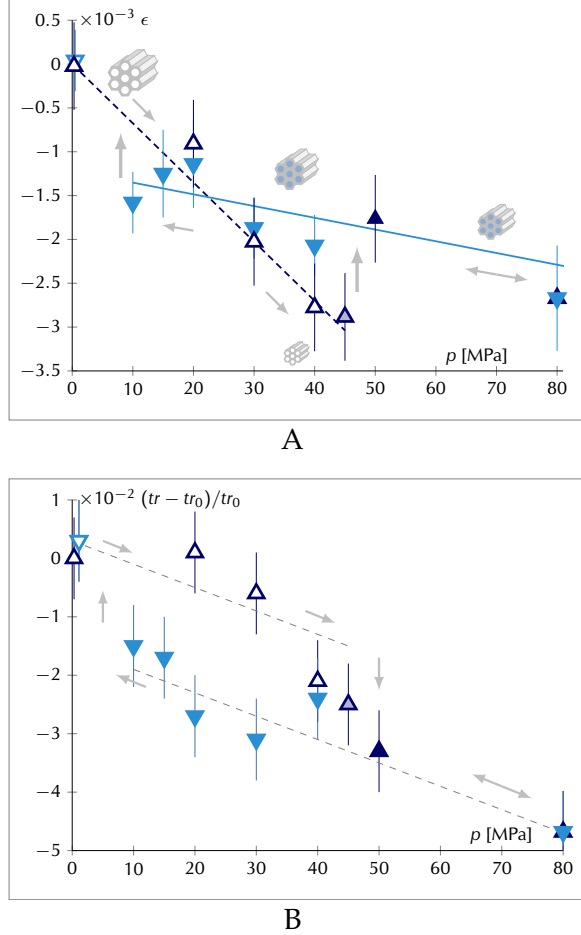


Figure 5: A) Deformation  $\epsilon$  plotted against the pressure  $p$  along an intrusion/extrusion cycle. Dark blue upward triangle: deformation measured when the pressure increases up to 80 MPa. Light blue downward triangle: deformation measured when the pressure decreases from 80 MPa. Empty symbols correspond to empty pores, filled symbols to filled pores. Dashed line: theoretical deformation for empty pores given by eq. 5. Full line: theoretical deformation for filled pores given by eq. 6. B) Relative variation of the transmission according to the pressure along an intrusion/extrusion cycle. Dashed gray lines indicate the relative variation of water amount due to isothermal compressibility before and after filling. Water intrusion occurs around 45 MPa while extrusion occurs below 10 MPa.

ing the pressure, this second trend is preserved down to 10 MPa while for the last measurement the transmission falls back close to its initial value. This hysteretic evolution of the transmission confirms that pores fill with water at around 45 MPa and expel water at around 10 MPa in agreement with the intrusometry cycle in Figure 2B. The extrusion pressure extracted from SANS measurement seems however slightly smaller than the one measured by intrusometry. A possible reason might be due to the ageing of the grafting used for the hydrophobization of the pores. In order to check that such

an ageing does not impact significantly our results, two independent series of measurement have been carried out with two samples. As recently shown with grafted periodic mesoporous material, ageing is mainly related to the time material spends filled in water<sup>19</sup>. Here, the first grafted MCM sample spent twice the time filled with water than the second sample. Once filled with water this second sample was used to characterize mesopores deformation at 10, 15, 30 and 40 MPa. Among the series of pressures studied with the filled first sample, the pressures 10, 30 and 40 MPa are common with the second sample. For each of these three pressures, the discrepancy between the measured deformation with the first and second samples remains in the limit of the measurement uncertainty. For these three particular pressures and for the measurements made when coming back to ambient pressure, the deformation shown in Figure 5A is the average of the deformation measured with these two samples, while other points correspond either to results obtained with the first or the second sample.

Based on the different measurements which confirm the pressure location for intrusion and extrusion, we separated our  $\epsilon$  values into two groups corresponding either to an empty state of the pores (empty symbols in Figure 5A) or a filled state of the pore (filled symbols in Figure 5A). Qualitatively, the slope of  $\epsilon$  with respect to the applied pressure  $p$  is significantly more pronounced for the empty state than for the filled state. To go beyond this qualitative description, a theoretical modeling is here useful for a quantitative characterization of the mechanical properties of our hydrophobic MCM-41 sample and a comparison with results previously obtained with pristine hydrophilic MCM-41.

### 3.2 Modeling of the deformation of superhydrophobic mesopores

The considered material corresponds to an almost perfect 2D hexagonal lattice of cylindrical pores of inner radius  $r_i$  and half distance between two adjacent pore centers  $r_0$ . As already suggested by several works<sup>6,7,9</sup>, this hexagonal lattice can be well approximated as the juxtaposition of tubes of inner radius  $r_i$  and outer radius  $r_0$ . This hypothesis inherently means that the deformation  $\epsilon$  is independent of the global size of the lattice. As a result, the deformation  $\epsilon$  is representative of the behavior of an individual tube submitted to an outer pressure  $p$  and an inner pressure  $p_i$ . To develop a simple model we assume the tube to be a perfect cylinder. The elastic behavior of the pore wall is restricted to the silica region only. The silane muffle is considered mechanically as a fluid layer with a free surface energy which depends on the nature of the fluid within the pore (either vapor or liquid). We finally consider that the lateral outer wall of the tube as well as its extremities are both submitted to the same outer pressure  $p$ . Under these hypothesis we aim at modeling the deformation  $\epsilon$  defined as the relative variation of the radius  $r_0$  when changing the outer pressure from  $p_r \simeq 0$  MPa (ambient pressure) to  $p$ . To calculate this relative variation we introduce the radial displacement  $u_r(r, p_i, p)$  within the tube wall according to the radius  $r$ , the pressure  $p_i$  acting on the inner wall thought the silane muffle (which differs from the

pressure of the fluid within the pore because of capillary and potentially disjoining effects) and the outer pressure  $p$  so that  $\epsilon = \Delta u_r(r_0)/r_0$ . As the considered individual tube is in fact embedded within the matrix, there is no real outer interface and in consequence no capillary or disjoining effects acting on this fictive external surface. The pressures  $p_i$  and  $p$  are linked to each other though the fluid equilibrium between the inside and the outside of the pore. At this stage however, to express  $u_r(r_0, p_i, p)$  in a general manner we keep  $p_i$  and  $p$  as independent pressures. From classical theory of elasticity<sup>35</sup> (see Supporting Information):

$$\frac{u_r(r_0, p_i, p)}{r_0} = \frac{1}{E} \left( \frac{2\phi}{1-\phi} p_i - \left( \frac{1+\phi}{1-\phi} - 2\nu \right) p + \frac{\phi}{1-\phi} \nu \Lambda \right) \quad (4)$$

with  $\phi = r_i^2/r_0^2$  the void fraction of the pores (i. e. the porosity) and  $\Lambda$  the averaged axial stress accounting for interfacial and contact line forces<sup>36</sup> which depends on the pressure  $p$  and on the state (either empty or filled) of the pore. In the following theoretical development surfaces stresses<sup>37</sup> are assumed as constant. Any dependence of surface stresses on surface strain<sup>38</sup> is neglected first because the considered strain are small and second because the uncertainty on our experimental data would not allow us to reveal such a dependence.

For a lyophobic inner wall and an empty pore, the inner fluid at pressure  $p_v$  is in a vapor state while the outer fluid at pressure  $p$  is in a liquid state. The equality of the chemical potential of the inner and outer fluids leads to:

$$p_v = p_{\text{sat}} \exp \left( \frac{(p - p_{\text{sat}})\mathcal{V}_l}{k_B T} \right)$$

where,  $p_{\text{sat}}$  is the saturation pressure at the considered temperature  $T$ ,  $k_B$  is the Boltzmann constant,  $\mathcal{V}_l$  is the molecular liquid volume. For  $p$  of the order of 40 MPa, the ratio  $p\mathcal{V}_l/(k_B T)$  is 0.35 and  $p_v$  is at most 45% larger than  $p_{\text{sat}}$  which is negligible with respect to  $p$ . For such an empty lyophobic mesopore, the liquid meniscus anchored at the extremity of the pore contributes to the pressure dependence of the axial force sustained by the silica elastic wall so that  $\Lambda - \Lambda_r = p$ , with  $\Lambda_r$  referring to the stress in the reference state at  $p_r \simeq 0$  MPa. In this situation, as  $p_v$  is negligible, the normal stress on the silica inner surface  $p_i$  is approximately constant and fixed by the pressure jump  $\gamma_{gv}/r_g$  across the curved silane/vapor interface (of surface tension  $\gamma_{gv}$ ) and the stress jump  $f_{sg}/r_i$  across the curved silica/silane interface (of surface stress  $f_{sg}$  involved in the Gurtin-Murdoch condition<sup>36,37</sup>). Here the disjoining pressure between silica walls, of the order of  $W_{\text{svs}}/(48\pi r_i^3) \sim 0.1$  MPa with  $W_{\text{svs}}$  the Hamaker constant of a silica/void/silica system<sup>39</sup> is fully negligible<sup>16</sup>. As a result, the deformation  $\epsilon_e(p)$  for an empty lyophobic pore expressed with respect to the reference state is:

$$\begin{aligned} \epsilon_e(p) &= -\frac{1}{E} \left( \frac{1+\phi}{1-\phi} - \left( 2 + \frac{\phi}{1-\phi} \right) \nu \right) p \\ &= -\frac{\alpha_e}{E} p \end{aligned} \quad (5)$$

with  $\alpha_e$  the  $\phi$  and  $\nu$ -dependent prefactor.

For a pore filled with liquid, the pressure of the inner liquid is equal to the pressure  $p$  of the outer liquid (neglecting disjoining pressure effects which are expected to be even smaller than in the empty case). For such a filled lyophobic mesopore, there is no more anchored meniscus and associated axial force but the transition from a silane/vapor to a silane/liquid interface leads to a jump of axial force with respect to the reference state so that  $\Lambda - \Lambda_r = (1 + r_g^2/r_i^2)(\gamma_{gl} - \gamma_{gv})/r_g$  with  $\gamma_{gl}$  the silane/liquid surface tension (see Supporting Information for further details). Due to this surface tension transition and to the inner pressure transition from  $p_v$  to  $p$ , the difference between the normal stress on the silica inner surface  $p_i$  and the reference value  $p_{ir}$  is  $p_i - p_{ir} = p - (\gamma_{gl} - \gamma_{gv})/r_g$ . Using the intrusion pressure  $p_{\text{int}}$ , which is expected to follow the Laplace law of capillarity<sup>28</sup>  $p_{\text{int}} = 2(\gamma_{gl} - \gamma_{gv})/r_g$ , the deformation  $\epsilon_f(p)$  of a filled pore is:

$$\begin{aligned} \epsilon_f(p) &= -\frac{1}{E} \left( (1-2\nu)p + \frac{\phi}{1-\phi} \left( 2 - \left( 1 + \frac{r_g^2}{r_i^2} \right) \nu \right) \frac{p_{\text{int}}}{2} \right) \\ &\simeq -\frac{1}{E} \left( \alpha_f p + \left( \alpha_e - \alpha_f \right) \frac{p_{\text{int}}}{2} \right) \end{aligned} \quad (6)$$

with  $\alpha_f = 1 - 2\nu$ . The approximation in the last expression consists in neglecting the  $r_g^2\nu/r_i^2$  term which corresponds to an error on the intercept position of the order of 5%. Such an approximation, which corresponds to a modest error in comparison to our experimental uncertainty, leads to a very simple model which fully captures the important trends of our experimental results. For both empty and filled states, the deformation decreases linearly with the pressure. Remarkably, the intercept of  $\epsilon_f$  is fixed by the intrusion pressure and the difference between the slopes of the deformation curves associated to filled and empty states. For empty pores the magnitude of the negative slope is  $K_e = \alpha_e/E$  while for filled pores it is  $K_f = -\alpha_f/E$ . Moreover from eqs 5 and 6 it is expected that  $\epsilon_e$  and  $\epsilon_f$  should be equal for  $p = p_{\text{int}}/2$ . This implies that the relaxation jump during intrusion is the opposite of the intercept of  $\epsilon_f$ , or  $(K_e - K_f)p_{\text{int}}/2$ . It is worth noting also that the Poisson ratio  $\nu$  appears as a simple function of these two slopes and of the porosity  $\phi$ :

$$\nu = \frac{K_e(1-\phi) - K_f(1+\phi)}{2K_e(1-\phi) - K_f(2-\phi)} \quad (7)$$

It is of interest to compare this simple theoretical behavior observed both in empty and filled states for lyophobic mesopores with the case of lyophilic mesopores (see Figure 6). For such a filled lyophilic mesopore, after capillary condensation, the equality of the chemical potential  $\mu$  of the inner liquid at pressure  $p_l$  and outer vapor at pressure  $p$  leads to  $p_l = p_{\text{sat}} + k_B T/\mathcal{V}_l \ln(p/p_{\text{sat}})$ . The vapor pressure  $p$  is in magnitude negligible with respect to the inner liquid pressure  $p_l$ . Comparing the filled state with the dry reference state  $p_i - p_{ir} = p_l - (f_{sl} - f_s)/r_i$  with  $f_{sl}$  the solid/liquid surface stress and  $f_s$  the bare solid surface stress. Axially there is this time a contribution of the meniscus limiting the confined liquid as well as a contribution of the surface stresses  $f_{sl}$  and  $f_s$  so that  $\Lambda - \Lambda_r = -p_l + 2(f_{sl} - f_s)/r_i$ . The deformation  $\epsilon_f$

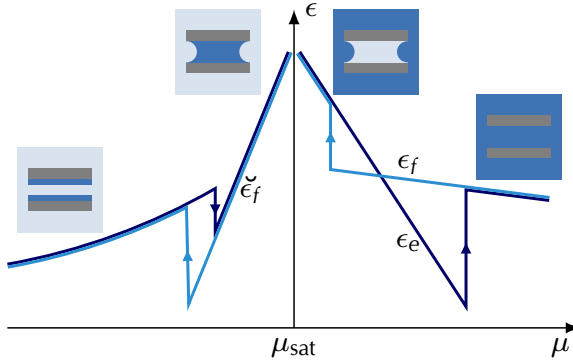


Figure 6: Schematics of the adsorption-induced deformation  $\epsilon$  of a lyophilic mesopore (left part  $\mu < \mu_{\text{sat}}$ ) and of the intrusion-induced deformation of lyophobic mesopore (right part  $\mu > \mu_{\text{sat}}$ ) according to the chemical potential  $\mu$  of the external fluid, either in a vapor state (left part) or in liquid state (right part). In both cases, dark lines correspond to pressure increase (adsorption or intrusion branch), light lines to pressure decrease (desorption or extrusion branch).

of the lyophilic filled pore, with respect to its dry state, writes from eq. 4

$$\check{\epsilon}_f(p) = \frac{\alpha_e - \alpha_f}{E} \left( p_l + \frac{2 - 2\nu}{2 - \nu} \frac{f_s - f_{sl}}{r_i} \right) \quad (8)$$

The inverse of the slope characterising the linear increase of  $\check{\epsilon}_f$  with  $p_l$  is  $M = E/(\alpha_e - \alpha_f) = E(\phi^{-1} - 1)/(2 - \nu)$ , previously introduced as the normal pore load modulus<sup>36</sup>. This *filled* lyophilic case (high outer vapor pressure) behaves anti-symmetrically to the *empty* hydrophobic state (low outer liquid pressure). In the lyophilic case,  $\check{\epsilon}_f$  increases linearly with the inner liquid pressure  $p_l$  whereas in the lyophobic case  $\epsilon_e$  decreases linearly with the outer liquid pressure  $p$ . Moreover the magnitude of the deformation observed in these two cases is larger than the one observed in the respective complementary states for a similar change of chemical potential (pre-wetting in the hydrophilic matrices at low outer vapor pressure, filled lyophobic matrix at large outer liquid pressure). For lyophilic and lyophobic matrices with identical geometries and wall mechanical properties one would expect, as typically  $\alpha_f \ll \alpha_e$ , that  $M$  (lyophilic case) is slightly larger than the modulus  $K_e^{-1}$  (lyophobic case). In the lyophilic case, the maximum dilation is reached at saturation for  $p = p_l = p_{\text{sat}}$  for which the deformation is directly related to the difference of surface stress<sup>20,36</sup>  $\check{\epsilon}_f(p_{\text{sat}}) \simeq M^{-1}(f_s - f_{sl})/r_i$  where  $f_s > f_{sl}$ . Similarly in the hydrophobic case the maximum compression is reached for  $p = p_{\text{int}}$  and  $\epsilon_f(p_{\text{int}}) = 2K_e(\gamma_{sv} - \gamma_{sl})/r_g$  where  $\gamma_{sv} < \gamma_{sl}$ .

The lyophilic case at low outer vapor pressure is however strongly different from the filled lyophobic case at high outer liquid pressure. In the lyophilic case, adsorption effects leads to the formation of a pre-wetting liquid film on the pore wall which has a significant impact on the pore deformation. Because of the presence of this pre-wetting film, a fully empty

state that would be analogous to the fully filled state observed in the lyophobic case does not exist. This is a major difference between these two cases. The modeling of this pre-wetting situation requires the proper description of disjoining pressure effects, thoroughly described in the literature, which generally implies the introduction of additional unknown physical parameters. The lyophobic case offers on the contrary the possibility to focus on the wall mechanics in both empty and filled states without the pitfall associated to the pre-wetting film description.

### 3.3 Comparison with experimental data

To determine the two coefficients  $K_e$  and  $K_f$  we proceed to a simultaneous least-square fitting of all our data. For empty pore points the deformation is modeled as  $\epsilon_e = -K_e p$  while for filled pore points we use  $\epsilon_f = -K_f p - (K_e - K_f)p_{\text{int}}/2$  with  $p_{\text{int}} = 45$  MPa. The resulting straight lines, which cross at  $p = p_{\text{int}}/2$  are shown in Figure 5A. The inverse of the so obtained coefficients, which can be compared to the pore load modulus, are  $K_e^{-1} = 15$  GPa and  $K_f^{-1} = 75$  GPa. Using eq. 7 we find  $\nu = 0.15 \pm 0.05$  which agrees with the typical value of 0.17 expected for amorphous silica<sup>23,40</sup>. Here the uncertainty is estimated from the uncertainty on the porosity  $\phi$  and on our measured deformations  $\epsilon$ . The ability to extract experimentally this Poisson ratio is a remarkable specificity of the lyophobic case which is free from the description of the pre-wetting regime. In the lyophilic case this ratio has to be imposed based on the assumed nature of the material. We confirm here that this value is a reasonable choice even for the nanometric thin wall of MCM-41. Based on this value we find  $\alpha_e = 3.5$  and  $\alpha_f = 1 - 2\nu = 0.7$ . We then deduce the Young's modulus of the matrix wall  $E = \alpha_e K_e^{-1} = 52 \pm 5$  GPa. This value is more explicitly shown in Figure 7 where all experimental points are plotted as a single master curve of slope  $E$ , using on the horizontal axis the negative measured deformation and on the vertical axis the stress  $\sigma$  expressed as  $\alpha_e p$  in the empty state and  $\alpha_f p - (\alpha_e - \alpha_f)p_{\text{int}}/2$  in the filled state. This Young's modulus value is also in good agreement with the value of 44 MPa found by Gor et al<sup>23</sup> based on the experiments of Prass et al<sup>6</sup> for pristine hydrophilic MCM-41 with a porosity  $\phi = 0.615$  similar to the one  $\phi = 0.6$  of our sample. The proximity of these two values confirms that our grafted sample is close to the pristine material, from a mechanical point of view, with a negligible impact of the grafting agent. Because of the slightly smaller Young's modulus and slightly larger porosity of Prass et al's sample, their load modulus  $M = 14$  MPa appears slightly smaller than  $K_e^{-1}$ . This trend is opposite to the one expected theoretically if the material properties would have been exactly the same.

These results complement a series of work on lyophilic mesopores<sup>7,21,48</sup> and confirms that the Young's modulus of MCM-41 wall is significantly smaller than the expected value of bulk silica of 73 GPa. Such a discrepancy is however not surprising taking into account the partial condensation of silica in MCM-41 walls<sup>47</sup>. To go beyond the specific case of MCM-41 we can refer to several recent studies aiming at characterizing the mechanical behavior of porous siliceous materials. In this context, several series of independent mea-

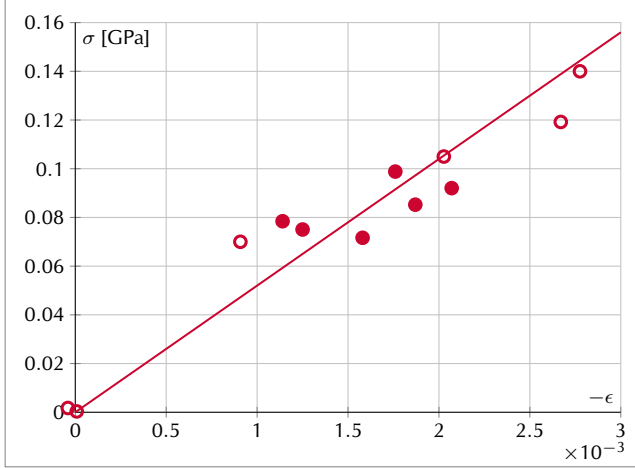


Figure 7: Stress  $\sigma$  applied to the mesopores according to the radial compression  $-\epsilon$ . Marks are experimental data with  $\sigma = \alpha_e p$  for empty pores (open symbols) and  $\sigma = \alpha_f p - (\alpha_e - \alpha_f)p_{int}/2$  for filled pores. The line is a linear regression the slope of which is the Young's modulus  $E = 52$  GPa.

surements, carried out on several types of siliceous materials, reveal a behavior close to a power law between the density of the material and its Young's modulus as shown in Figure 8. In order to compare the case of MCM-41 to this trend, we use the numerical work of Coasne et al<sup>47</sup> to estimate the average density within the silica walls MCM-41 as (see inset of Figure 8). From the density distribution proposed by these authors we find an average density of  $1.8 \text{ g.cm}^{-3}$ . This density associated with the value of Young's modulus used in our mechanical model defines a point which is well positioned within the cluster of points in Figure 8. This last result suggests that the empirical power law between Young's modulus and silica density is valid down to nanometric thin structures such as the walls of MCM-41 considered in this study.

## 4 Conclusion

A high pressure set-up dedicated to intrusion/extrusion studies of water in model hydrophobic nanopores combined with small angle neutron scattering measurements provides an unprecedented approach to study the local deformation of superhydrophobic mesopores during an intrusion/extrusion cycle. A hysteretic strain isotherm is observed which stands out from the typical strain isotherm measured with hydrophilic mesopores. We obtain a bowtie-shaped isotherm comprising two distinct linear branches before and after forced filling of the pores. The superhydrophobic matrix is either filled in vapor, without liquid adsorption on the pore walls, at a pressure slightly larger than the saturation pressure, or filled with liquid, at the same pressure as the outer bulk liquid once forced filling as occurred. The mechanical response of vapor filled mesopores surrounded with liquid is comparable to the one of liquid filled hydrophilic mesopores surrounded with vapor. However the mechanical response

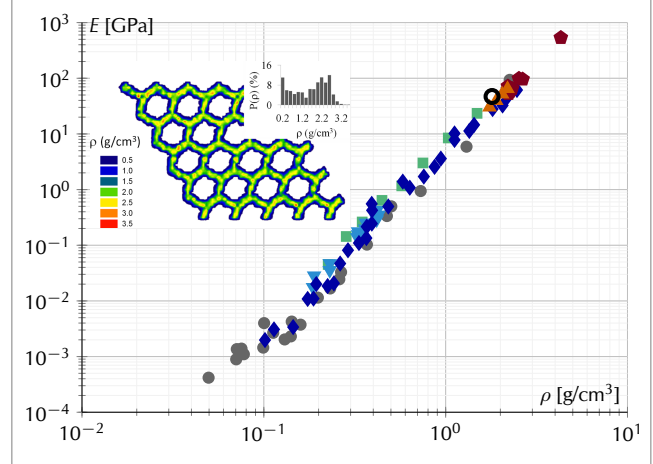


Figure 8: Young's modulus  $E$  for different types of silica samples (aerogel, xerogel, silica glass, cristobalite, quartz) according to their density  $\rho$ . Data are collected from several authors, gray dots<sup>41</sup>, diamond<sup>42</sup>, blue triangle<sup>43</sup>, square<sup>44</sup>, orange triangle<sup>45</sup>, pentagon<sup>46</sup>. The black open circle is our measurement with an averaged density estimated from the work by Coasne et al<sup>47</sup>. The inset is a replica of the Figure 8 of this work showing a density map of the silica walls of an atomistic structural model of MCM-41 material.

of liquid filled hydrophobic pores depart from the one of partially empty hydrophilic pores where adsorption as a strong mechanical impact. The absence of pre-wetting film and associated disjoining pressure effects in the hydrophobic case constitutes a major difference with respect to the hydrophilic case and leads to a simple mechanical modeling of pore deformation in both empty and filled states. Once the intrusion pressure is known it turns out that the strain isotherm of hydrophobic cylindrical mesopores is fully defined by the Young's modulus and the Poisson ratio of pore walls without any additional parameters. Reversely, the characterization of the strain isotherm of hydrophobic pores gives the ability to experimentally determine these two parameters, in particular the Poisson ratio which can not be directly obtained from the strain isotherm of hydrophilic pores. In the case of silanized MCM-41 we find a Poisson ratio of 0.15 which is very close to the value of 0.17 generally used for amorphous silica. The Young's modulus of 52 MPa is close from the one of 44 MPa previously found for similar pristine MCM-41. Such a moderate value with respect to bulk silica reveals nevertheless in agreement with the typical trend observed for the Young's modulus according to the density of various siliceous material. Our results suggest that, from a mechanical point of view, the nanometric thin wall of MCM-41 matrix behaves similarly to macroscopic siliceous material presenting the same density. This work opens the route to the local characterization of the mechanical properties of nanostructured hydrophobic material and certainly to a more detail description of the specific mechanical contribution of the grafting.

**Acknowledgement** The authors thank the Institut Laue-

Langevin (Grenoble, France) for the allocation of neutron beam time. The neutron data set is available at doi:10.5291/ILL-DATA.6-07-24. This work was supported by the French Research Agency (ANR LyStEn 15-CE06-0006). We thank Claude Payre for high pressure equipment and the design of the high pressure cell as well as Olivier Aguettaz for the technical support during the experiment. We thank Christophe Martin and Charles Josserond for the access to traction machine at the SIMAP/GPM2 laboratory needed for intrusiometry experiments, Stéphane Coindeau for X-ray characterization and Vincent Martin for nitrogen adsorption and TGA analysis. Finally we thank Benoit Coasne for fruitful discussion concerning the silica structure of MCM-41 matrices.

## Supporting Information Available

The following files are available free of charge. Description of the high pressure setup fo SANS experiments.  
Mechanical model for pore deformation.  
Pore size characterisation.

## References

- (1) Coussy, O. *Mechanics and Physics of Porous Solids*; John Wiley & Sons, 2010.
- (2) Coudert, F.-X.; Boutin, A.; Fuchs, A. H.; Neimark, A. V. Adsorption Deformation and Structural Transitions in Metal-Organic Frameworks: From the Unit Cell to the Crystal. *The Journal of Physical Chemistry Letters* **2013**, *4*, 3198–3205.
- (3) Honorio, T.; Brochard, L.; Vandamme, M.; Paris-est, U.; Umr, L. N.; Pascal, A. B. Hydration Phase Diagram of Clay Particles from Molecular Simulations. *Langmuir* **2017**, *33*, 12766–12776.
- (4) Chen, M.; Coasne, B.; Guyer, R.; Derome, D.; Carmeliet, J. Role of hydrogen bonding in hysteresis observed in sorption-induced swelling of soft nanoporous polymers. *Nature Communications* **2018**, *9*.
- (5) Günther, G.; Prass, J.; Paris, O.; Schoen, M. Novel Insights into Nanopore Deformation Caused by Capillary Condensation. *Physical Review Letters* **2008**, *101*, 20–23.
- (6) Prass, J.; Müter, D.; Fratzl, P.; Paris, O. Capillarity-driven deformation of ordered nanoporous silica. *Applied Physics Letters* **2009**, *95*, 1–3.
- (7) Gor, G. Y.; Bertinetti, L.; Bernstein, N.; Hofmann, T.; Fratzl, P.; Huber, P. Elastic response of mesoporous silicon to capillary pressures in the pores. *Applied Physics Letters* **2015**, *106*, 1–5.
- (8) Rolley, E.; Garroum, N.; Grosman, A. Using capillary forces to determine the elastic properties of mesoporous materials. *Physical Review B* **2017**, *96*, 064106, 1–7.
- (9) Ludescher, L.; Morak, R.; Balzer, C.; Waag, A. M.; Braxmeier, S.; Putz, F.; Busch, S.; Gor, G. Y.; Neimark, A. V.; Hu, N.; Reichenauer, G.; Paris, O. In Situ Small-Angle Neutron Scattering Investigation of Adsorption- Induced Deformation in Silica with Hierarchical Porosity. *Langmuir* **2019**, *35*, 11590–11600.
- (10) Tortora, M.; Zajdel, P.; Lowe, A. R.; Jensen, G. V.; Bleuel, M.; Giacomello, A.; Casciola, C. M.; Meloni, S.; Grosu, Y. Giant Negative Compressibility by Liquid Intrusion into Superhydrophobic Flexible Nanoporous Frameworks. *Nano Letters* **2021**, *21*, 2848–2853.
- (11) Zajdel, P.; Chorazewski, M.; Leão, J. B.; Jensen, G. V.; Bleuel, M.; Zhang, H.-f.; Feng, T.; Luo, D.; Li, M.; Lowe, A. R.; Geppert-rybczynska, M.; Li, D.; Grosu, Y. Inflation Negative Compressibility during Intrusion-Extrusion of a Non-Wetting Liquid into a Flexible Nanoporous Framework. *The Journal of Physical Chemistry Letters* **2021**, *12*, 4951–4957.
- (12) Neimark, A. V.; Triguero, C.; Boutin, A.; Fuchs, A. H.; Beurroies, I.; Denoyel, R. Structural Transitions in MIL-53 ( Cr ): View from Outside and Inside. *Langmuir* **2011**, *53*, 4734–4741.
- (13) Fadev, A. Y.; Eroshenko, V. Study of Penetration of Water into Hydrophobized Porous Silicas. *Journal of colloid and interface science* **1997**, *187*, 275–282.
- (14) Eroshenko, V.; Regis, R.-C.; Soulard, M.; Parain, J. Energetics : A New Field of Applications for Hydrophobic Zeolites. *Journal of American Chemical Society* **2001**, *123*, 8129–8130.
- (15) Grosu, Y.; Renaudin, G.; Eroshenko, V.; Nedelec, J.-M.; Grolier, J.-P. Synergetic effect of temperature and pressure on energetic and structural characteristics of ZIF-8 + water molecular spring. *Nanoscale* **2015**, *7*, 8803–8810.
- (16) Guillemot, L.; Biben, T.; Galarneau, A.; Vigier, G.; Charlaix, E. Activated drying in hydrophobic nanopores and the line tension of water. *Proceedings of the National Academy of Sciences* **2012**, *109*, 19557.
- (17) Tinti, A.; Giacomello, A.; Grosu, Y.; Casciola, C. M. Intrusion and extrusion of water in hydrophobic nanopores. *Proceedings of the National Academy of Sciences* **2017**, *20266–10273*.
- (18) Fraux, G.; Coudert, F.-X.; Boutin, A.; Fuchs, A. H. Forced intrusion of water and aqueous solutions in microporous materials: from fundamental thermodynamics to energy storage devices. *Chem. Soc. Rev.* **2017**, *7421–7437*.
- (19) Picard, C.; Gerard, V.; Michel, L.; Xavier, C.; Charlaix, E. Dynamics of heterogeneous wetting in periodic hybrid nanopores. *Journal of Chemical Physics* **2021**, *154*, 1–11.

- (20) Gor, G. Y.; Neimark, A. V. Adsorption-Induced Deformation of Mesoporous Solids. *Langmuir* **2010**, *26*, 13021–13027.
- (21) Schoen, M.; Paris, O.; Günther, G.; Müter, D.; Prass, J.; Fratzl, P. Pore-lattice deformations in ordered mesoporous matrices: experimental studies and theoretical analysis. *Physical chemistry chemical physics : PCCP* **2010**, *12*, 11267–11279.
- (22) Gor, G. Y.; Paris, O.; Prass, J.; Russo, P. A.; Ribeiro Carrott, M. M. L.; Neimark, A. V. Adsorption of n-pentane on mesoporous silica and adsorbent deformation. *Langmuir* **2013**, *29*, 8601–8608.
- (23) Gor, G. Y.; Huber, P.; Bernstein, N. Adsorption-induced deformation of nanoporous materials - A review. *Applied Physics Reviews* **2017**, *4*.
- (24) Guillemot, L.; Galarneau, A.; Vigier, G.; Abensur, T.; Charlaix, É. New device to measure dynamic intrusion / extrusion cycles of lyophobic heterogeneous systems. *Review of Scientific Instruments* **2012**, *83*, 1–8.
- (25) Briggs, H.; Sinha, R. P. Expansion and Contraction of Coal caused respectively by the Sorption and Discharge of Gas. *Proceedings of the Royal Society of Edinburgh* **1934**, *53*, 48–53.
- (26) Sanz, A.; Hansen, W.; Jakobsen, B.; Pedersen, I. H.; Capaccioli, S.; Adrjanowicz, K.; Paluch, M.; Gonthier, J.; Frick, B.; Lelièvre-Berna, E.; Peters, J.; Niss, K. High-pressure cell for simultaneous dielectric and neutron spectroscopy. *Review of Scientific Instrument* **2018**, *89*, 1–9.
- (27) Wolanin, J.; Giraud, J.; Payre, C.; Benoit, M.; Antonelli, C.; Quemener, D.; Vandamme, M.; Zanotti, J.-m.; Plazanet, M. Oedometric-like setup for the study of water transport in porous media by quasi- elastic neutron scattering. *Review of Scientific Instrument* **2021**, *92*, 1–9.
- (28) Lefevre, B.; Saugey, A.; Barrat, J. L.; Bocquet, L.; Charlaix, E.; Gobin, P. F.; Vigier, G. Intrusion and extrusion of water in hydrophobic mesopores. *Journal of Chemical Physics* **2004**, *120*, 4927–4938.
- (29) di Meglio, J.-M.; Quere, D.; Brochard-Wyart, F. Films mouillants dans les capillaires. *Compte-Rendu de l'Académie des Sciences* **1989**, *309*, 19–24.
- (30) Pellenq, R. J.; Coasne, B.; Denoyel, R. O.; Coussy, O. Simple phenomenological model for phase transitions in confined Geometry. 2. Capillary condensation/evaporation in cylindrical mesopores. *Langmuir* **2009**, *25*, 1393–1402.
- (31) Deroche, I.; Daou, T. J.; Picard, C.; Coasne, B. Reminiscent capillarity in subnanopores. *Nature Communications* **2019**, *10*, 1–10.
- (32) Michel, L. Etude macroscopique dynamique et microscopique des systèmes hétérogènes lyophobes. Ph.D. thesis, Université Grenoble Alpes, 2019.
- (33) Prass, J.; Müter, D.; Erko, M.; Paris, O. Apparent lattice expansion in ordered nanoporous silica during capillary condensation of fluids. *Journal of Applied Crystallography* **2012**, *45*, 798–806.
- (34) Morak, R.; Braxmeier, S.; Ludescher, L.; Putz, F.; Busch, S.; Hüsing, N.; Reichneauer, G.; Paris, O. Quantifying adsorption-induced deformation of nanoporous materials on different length scales research papers. *Journal of Applied Crystallography* **2017**, *50*, 1404–1410.
- (35) Timoshenko, S.; Goodier, J. *Theory of Elasticity*, 3rd ed.; McGraw-Hill, 1970.
- (36) Gor, G. Y.; Huber, P.; Weissmüller, J. Elastocapillarity in nanopores: Sorption strain from the actions of surface tension and surface stress. *Physical Review Materials* **2018**, *2*, 1–17.
- (37) Kramer, D.; Weissmuller, J. A note on surface stress and surface tension and their interrelation via Shuttleworth's equation and the Lippmann equation. *Surface Science* **2007**, *601*, 3042–3051.
- (38) Xu, Q.; Jensen, K. E.; Boltynskiy, R.; Sarfati, R.; Style, R. W.; Dufresne, E. R. Direct measurement of strain-dependent solid surface stress. *Nature Communications* **2017**, *8*, 1–6.
- (39) Israelachvili, J. *Intermolecular and Surface Forces*; Elsevier, 2011.
- (40) Greaves, G. N.; Greer, A. L.; Lakes, R. S.; Rouxel, T. Poisson's ratio and modern materials. *Nature Materials* **2011**, *10*, 823–837.
- (41) Cross, J.; Goswin, R.; Gerlach, R.; Fricke, J. Mechanical properties of SiO<sub>2</sub> aerogel. *Revue de Physique Appliquée* **1989**, *24*, 185–190.
- (42) Woignier, T.; Reynes, J.; Hafidi Alaoui, A.; Beurroies, I.; Phalippou, J. Different kinds of structure in aerogels: Relationships with the mechanical properties. *Journal of Non-Crystalline Solids* **1998**, *241*, 45–52.
- (43) Woignier, T.; Pelous, J.; Phalippou, J.; Vacher, R.; Courtens, E. Elastic properties of silica aerogels. *Journal of Non-Crystalline Solids* **1987**, *95*, 1197–1202.
- (44) Murillo, J. S.; Bachlechner, M. E.; Campo, F. A.; Barbero, E. J. Structure and mechanical properties of silica aerogels and xerogels modeled by molecular dynamics simulation. *Journal of Non-Crystalline Solids* **2010**, *356*, 1325–1331.

- (45) Campbell, T.; Kalia, R. K.; Nakano, A.; Shimojo, F.; Tsuruta, K.; Vashishta, P.; Ogata, S. Structural Correlations and Mechanical Behavior in Nanophase Silica Glasses. *Physical Review Letters* **1999**, *82*, 4018–4021.
- (46) Pabst, W.; Gregorová, E. Elastic properties of silica polymorphs – a review. *Ceramics - Silikaty* **2013**, *57*, 167–184.
- (47) Coasne, B.; Ugliengo, P. Atomistic Model of Micelle-Templated Mesoporous Silicas : Structural , Morphological , and Adsorption Properties. *Langmuir* **2012**, *28*, 11131–11141.
- (48) Balzer, C.; Waag, A. M.; Gehret, S.; Reichenauer, G.; Putz, F.; Hu, N.; Paris, O.; Bernstein, N.; Gor, G. Y.; Neimark, A. V. Adsorption-Induced Deformation of Hierarchically Structured Mesoporous Silica - Effect of Pore-Level Anisotropy. *Langmuir* **2017**, *33*, 5592–5602.

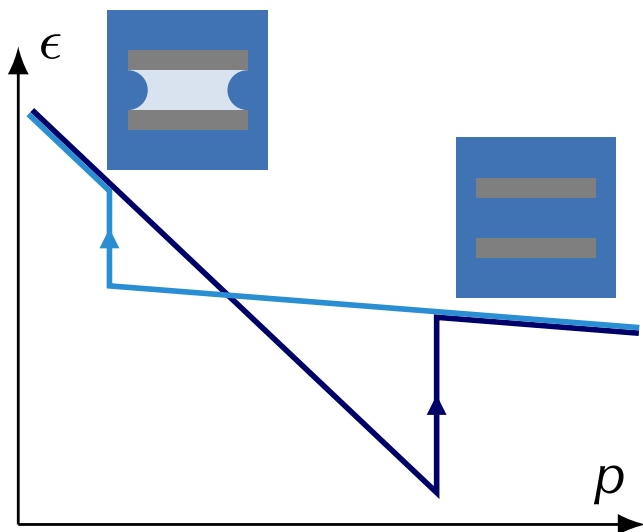


Figure 9: For Table of Contents Use Only

# The bowtie-shaped deformation isotherm of superhydrophobic cylindrical mesopores: Supporting Information

Loïc Michel,<sup>†</sup> Lukas Ludescher,<sup>‡</sup> Viviana Cristiglio,<sup>¶</sup> Elisabeth Charlaix,<sup>†</sup> Oskar Paris,<sup>‡</sup> and Cyril Picard<sup>\*,†</sup>

<sup>†</sup>Univ. Grenoble Alpes, CNRS, LIPhy, 38000 Grenoble, France

<sup>‡</sup>Institute of Physics, Montanuniversitaet Leoben, Franz-Josef-Strasse 18, 8700 Leoben, Austria

<sup>¶</sup>Institut Laue Langevin, 38042 Grenoble, France

E-mail: cyril.picard@univ-grenoble-alpes.fr

## High pressure set up

Experiments were carried out with a cylindrical cell (19PL10AL6, figure 1A and 1B) specifically tailored to our needs. The cell is made of an aluminum alloy with optimal mechanical properties (7049, MgZn2 precipitation) enclosing a lightly alloyed aluminum insert with 3% magnesium (AG3, 5754, figure 1A) maximizing neutron transparency. The cell can be operated up to 100 MPa with temperature up to 50°C.

The insert was designed to accommodate both SANS constraints and the rheological behaviour of the dense wetted powder behaving as a paste. The insert comprises a shallow parallelipipedic slit containing the sample. As a result, the sample presents a plane geometry which avoids corrections needed in cylindrical geometry. To simplify the filling of the slit the insert is open along its outer lateral cylindrical surface. Such an aperture is also of interest to maximise the width of the sample (which is equal to the diameter of the insert). Filling of the insert is done by using a spatula to force the wetted paste within the parallelipipedic slit. The insert is oriented within the high pressure cell so that to maximise the intensity of Bragg picks. The entire measurement system is shown in figure S2.

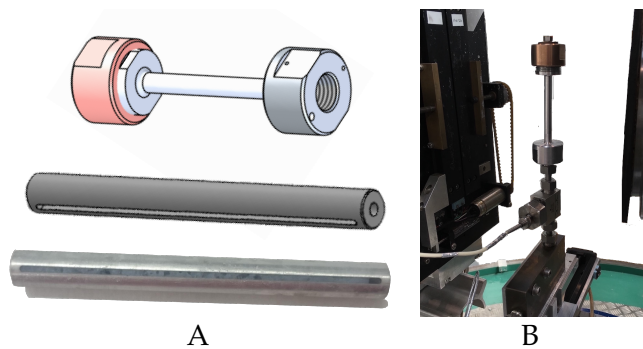


Figure S1: A) Schematics of the cell and of the insert and picture of the insert filled with the wetted MCM-41 powder behaving as a paste. B) Picture of the cylindrical high pressure cell mounted on the diffractometer above the fluid separator and pressure sensor.



Figure S2: Picture of the setup with the pressure-regulated syringe pump (right hand side) and the thermally regulated chamber enclosing the cell.

## Thick-wall pore deformation

From the fundamental law of thermodynamics

$$\rho \frac{\partial^2 u}{\partial t^2} = \nabla \cdot (\sigma) + f_v$$

where  $u$  is the displacement,  $\sigma$  is the stress tensor and  $f_v$  are volume forces. Using Hooke's law,

$$\sigma = \lambda \text{tr}(\epsilon) I + 2\mu \epsilon$$

the Navier equation results, which expresses the mechanical balance according to the displacement  $u$ <sup>1,2</sup>

$$\rho \frac{\partial^2 u}{\partial t^2} = (\lambda + 2\mu) \vec{\nabla} \left( \vec{\nabla} \cdot \vec{u} \right) - \mu \vec{\nabla} \wedge \left( \vec{\nabla} \wedge \vec{u} \right) + \vec{f}_v$$

where  $\lambda$  and  $\mu$  are the Lamé coefficients. In absence of volume force and at equilibrium

$$(\lambda + 2\mu) \vec{\nabla} \left( \vec{\nabla} \cdot \vec{u} \right) - \mu \vec{\nabla} \wedge \left( \vec{\nabla} \wedge \vec{u} \right) = \vec{0}$$

For a cylinder submitted to axisymmetric forces, the displacement is independent of the azimuthal coordinate. In absence of buckling, the radial displacement  $u_r$  is a function of the radius  $r$  only and the longitudinal displacement  $u_z$  is a function of the longitudinal coordinate  $z$  only, that is  $\vec{\nabla} \wedge \vec{u} = \vec{0}$ . This implies  $\vec{\nabla} \cdot \vec{u} = \text{constant}$ . In cylindrical coordinates this means

$$\frac{1}{r} \frac{\partial}{\partial r} (r u_r) + \frac{\partial u_z}{\partial z} = \text{constant}$$

As the first term is a function of  $r$  only and the second term a function of  $z$  only this implies

$$\begin{aligned} \frac{\partial(r u_r)}{\partial r} &= 2ar \\ \frac{\partial u_z}{\partial z} &= c \end{aligned}$$

where  $a$  and  $c$  are two constants. After integration:

$$\begin{aligned} u_r &= ar + \frac{b}{r} \\ u_z &= cz + d \end{aligned}$$

where  $b$  and  $d$  are two integration constants. The corresponding strain are:

$$\begin{aligned} \varepsilon_{rr} &= a - \frac{b}{r^2} \\ \varepsilon_{\theta\theta} &= a + \frac{b}{r^2} \\ \varepsilon_{zz} &= c \end{aligned}$$

and off diagonal components are zero. Using Hooke's law, one obtains

$$\begin{aligned} \sigma_{rr} &= A - \frac{B}{r^2} \\ \sigma_{\theta\theta} &= A + \frac{B}{r^2} \\ \sigma_{zz} &= C \end{aligned}$$

with off diagonal components equal to zero, and with

$$\begin{aligned} A &= 2(\lambda + \mu)a + \lambda c \\ B &= 2\mu b \\ C &= 2\lambda a + (\lambda + 2\mu)c \end{aligned}$$

That is

$$\begin{aligned} A(\lambda + 2\mu) - \lambda C &= 2((\lambda + \mu)(\lambda + 2\mu) - \lambda^2)a \\ &= 2\mu(3\lambda + 2\mu)a \\ B &= 2\mu b \\ A\lambda - C(\lambda + \mu) &= (\lambda^2 - (\lambda + 2\mu)(\lambda + \mu))c \\ &= -(\mu(3\lambda + 2\mu))c \end{aligned}$$

Using the expressions of  $\lambda$  and  $\mu$  according to the Young modulus  $E$  and the Poisson ratio  $\nu$

$$\begin{aligned} \frac{1}{E} &= \frac{\lambda + \mu}{\mu(3\lambda + 2\mu)} \\ \frac{\nu}{E} &= \frac{\lambda}{2\mu(3\lambda + 2\mu)} \\ \frac{1}{\mu} &= \frac{2(1 + \nu)}{E} \end{aligned}$$

one gets:

$$\begin{aligned} a &= \frac{1 - \nu}{E}A - \frac{\nu}{E}C \\ b &= \frac{1 + \nu}{E}B \\ c &= \frac{C}{E} - \frac{2\nu}{E}A \end{aligned}$$

For a tube with thick walls submitted on its outer wall and on its annular base, to a uniform outer pressure  $p_o$  and on its inner wall to a pressure  $p_i$  (which can be related to surface stress contributions<sup>3,4</sup>), the boundary conditions leads to

$$\begin{aligned} A &= \frac{p_o r_o^2 - p_i r_i^2}{r_i^2 - r_o^2} \\ B &= (p_o - p_i) \frac{r_o^2 r_i^2}{r_i^2 - r_o^2} \\ C &= -p_o - \Lambda \frac{r_i^2}{r_o^2 - r_i^2} \end{aligned}$$

where  $\Lambda$  corresponds to the averaged axial stress accounting for interfacial and contact line forces<sup>3</sup>. Consequently

$$\begin{aligned} a &= \frac{(1 - \nu)(p_o r_o^2 - p_i r_i^2)}{E(r_i^2 - r_o^2)} + \frac{\nu}{E} \left( p_o + \Lambda \frac{r_i^2}{r_o^2 - r_i^2} \right) \\ b &= \frac{1 + \nu}{E} (p_o - p_i) \frac{r_o^2 r_i^2}{r_i^2 - r_o^2} \\ c &= \frac{2\nu(p_o r_o^2 - p_i r_i^2)}{E(r_o^2 - r_i^2)} - \frac{1}{E} \left( p_o + \Lambda \frac{r_i^2}{r_o^2 - r_i^2} \right) \end{aligned}$$

The relative radius variation of the outer surface is finally<sup>1,2</sup>

$$\begin{aligned} \frac{u_r(r_o)}{r_o} &= a + \frac{b}{r_o^2} \\ &= \frac{(1 - \nu)(p_o r_o^2 - p_i r_i^2) + (1 + \nu)(p_o - p_i)r_i^2}{E(r_i^2 - r_o^2)} \\ &\quad + \frac{\nu}{E} \left( p_o + \Lambda \frac{r_i^2}{r_o^2 - r_i^2} \right) \\ &= \frac{1}{E} \left( \frac{2r_i^2}{r_o^2 - r_i^2} p_i - \left( \frac{r_o^2 + r_i^2}{r_o^2 - r_i^2} - 2\nu \right) p_o \right) + \frac{\nu}{E} \Lambda \frac{r_i^2}{r_o^2 - r_i^2} \end{aligned}$$

The pressure  $p_i$  (or more rigorously the normal component of the surface stress on the surface of radius  $r_i$ ) is obtained combining by the Gurtin-Murdoch condition (for solid/fluid interfaces) and the Laplace law of capillarity (for fluid/fluid

interfaces). For empty lyophilic ungrafted mesopores (neglecting wall fluid wall disjoining pressure):

$$p_i = -\frac{f_s}{r_i}$$

$$\Lambda = 2\frac{f_s}{r_i}$$

where  $f_s$  is the surface stress on the bare internal wall. For a lyophilic pore covered with a fluid pre-wetting film of thickness  $t$

$$p_i = p - \frac{\gamma_{lv}}{r_i - t} - \frac{f_{sl}}{r_i}$$

$$\Lambda = 2 \left( \frac{f_{sl}}{r_i} + \gamma_{lv} \frac{r_i - t}{r_i^2} \right) - p_l \left( 1 - \left( 1 - \frac{t}{r_i} \right)^2 \right)$$

where  $\gamma_{lv}$  is the liquid/vapor surface tension,  $f_{sl}$  is the surface stress at the solid/liquid interface and  $p_l$  is the pressure within the liquid film which can be expressed, at thermodynamical equilibrium from the chemical potential fixed by the vapor pressure  $p_v$ .

For a lyophilic pore filled in liquid

$$p_i = p_l - \frac{f_{sl}}{r_i}$$

$$\Lambda = 2\frac{f_{sl}}{r_i} - p_l$$

For an empty lyophobic grafted pore (neglecting the mechanical contribution of the inner vapor pressure  $p_v$ ) with a silane layer of thickness  $t_g$  (assumed to be constant) immersed in liquid at pressure  $p$

$$p_i = -\frac{\gamma_{gv}}{r_i - t} - \frac{f_{sg}}{r_i}$$

$$\Lambda = 2 \left( \frac{f_{sg}}{r_i} + \gamma_{gv} \frac{r_g}{r_i^2} \right) - p_g \left( 1 - \frac{r_g^2}{r_i^2} \right) + p$$

$$= 2\frac{f_{sg}}{r_i} + \frac{\gamma_{gv}}{r_g} \left( 1 + \frac{r_g^2}{r_i^2} \right) + \Pi_v \left( 1 - \frac{r_g^2}{r_i^2} \right) + p \frac{r_g^2}{r_i^2}$$

where  $\gamma_{gv}$  is the surface tension of the silane/vapor interface,  $f_{sg}$  is the surface stress at the solid/silane interface,  $p_g$  is the pressure within the grafting agent layer and  $\Pi$  the disjoining pressure associated to the silane layer.

For a filled lyophobic grafted pore

$$p_i = p - \frac{\gamma_{lv}}{r_i - t} - \frac{f_{sg}}{r_i}$$

$$\Lambda = 2 \left( \frac{f_{sg}}{r_i} + \gamma_{gl} \frac{r_g}{r_i^2} \right) + (p - p_g) \left( 1 - \frac{r_g^2}{r_i^2} \right)$$

$$= 2\frac{f_{sg}}{r_i} + \frac{\gamma_{gl}}{r_g} \left( 1 + \frac{r_g^2}{r_i^2} \right) + \Pi_l \left( 1 - \frac{r_g^2}{r_i^2} \right)$$

where  $\gamma_{gl}$  is the surface tension of the silane/liquid interface. The difference in  $\Lambda$  values between the filled state and the empty reference state comprises a disjoining pressure term

$(\Pi_l - \Pi_v)(1 - r_g^2/r_i^2)$  across the silane layer that is negligible with respect to the surface tension term. The difference in disjoining pressure can be estimated from the derivative of the surface energy with respect to the thickness of the silane layer  $\Pi_l - \Pi_v = -d(\gamma_{gl} - \gamma_{gv})/dt_g = -d(p_{intrg}/2)/dt_g$ . To get an order of magnitude, we compare our results with the one by Lefevre *et al*<sup>11</sup>. In their sample the thickness  $t_g$  was estimated to be 0.5 nm for a coverage density of  $1.3 \text{ nm}^{-2}$  corresponding to a radius  $r_g = r_i - t_g = 1.3 \text{ nm}$  and a measured intrusion pressure of 60 MPa. As our coverage density is twice less than the one of Lefevre *et al* we estimate crudely that for our sample the effective thickness is  $t_g \sim 0.25 \text{ nm}$  and  $r_g = r_i - t_g \sim 1.5 \text{ nm}$ , while the measured intrusion pressure is 45 MPa. Consequently we find  $\Pi_l - \Pi_v \sim -16 \text{ MPa}$ . Consequently, as  $r_g$  is close to  $r_i$ , the term  $(\Pi_l - \Pi_v)(1 - r_g^2/r_i^2)$  is expected to be one order of magnitude smaller than the term  $(\gamma_{gl} - \gamma_{gv})/r_g(1 + r_g^2/r_i^2) = p_{int}(1 + r_g^2/r_i^2)/2$ .

## Pore size characterisation

The inner pore radius of the pristine material is deduced from nitrogen adsorption using a Derjaguin-Broekhoff-de Boer analysis<sup>5-7</sup>. At low relative pressure a pre-wetting film of thickness  $t < r$  is supposed to cover a pore of radius  $r$ . The grand potential  $\Omega$  in this pre-wetting regime depends on the film thickness. The equilibrium of the liquid film corresponds to a minimum of the grand potential or  $\partial\Omega/\partial t = 0$  at fixed chemical potential<sup>7</sup>. In the framework of the Derjaguin approximation, we consider a surface potential  $W_{slv}$  term in  $\Omega$  to model the vapor solid interactions through the liquid film. Following several previous studies, the surface potential is expressed as an exponential decay  $W_{slv} = S \exp(-t/\xi)$  where  $S$  is the spreading parameter and  $\xi$  an interaction length. With such a form for  $W_{slv}$ , we calculate the film thickness  $t(p_v)$  so that  $\Omega$  is minimum<sup>8-10</sup>. The thickness is expected to jumps from  $t < r$  to  $t = r$  when  $\Omega(t < r) = \Omega(r)$  that is the thermodynamical equilibrium defining capillary condensation.

The fluid amount in a pore of radius  $r$  and length  $L$  at pressure  $p_v$  can be approximated by the liquid amount in this pore  $V(p_v, r) = \pi L r^2 (1 - (1 - t(r, p_v)/r)^2)$ . Considering a bundle of cylindrical pores with a Gaussian distribution of average radius  $r_i$  and standard deviation  $\sigma$

$$V(p_v) = \lambda L \int \pi r^2 \left( 1 - (1 - t(r, p_v)/r)^2 \right) e^{-\left(\frac{r-r_i}{\sqrt{2}\sigma}\right)^2} dr \quad (1)$$

with  $\lambda$  a dimensionless parameter such that the total volume of the pore  $V_p$  is

$$V_p = \lambda L \int r^2 e^{-\left(\frac{r-r_p}{\sqrt{2}\sigma}\right)^2} dr$$

In our analysis the experimental value of  $V_p$  is defined as the volume reached at the end of the condensation jump. Based on this model fitted on our experimental points we obtained the continuous red curve, in the inset of Figure 2A) of the article. This model has four independent parameters. We find  $S = 0.068 \pm 0.002 \text{ J/m}^2$  and  $\xi = 0.20 \pm 0.01 \text{ nm}$  mostly fixed by the pre-wetting regime,  $r_m$  the average pore radius fixed

by the position of the condensation jump and  $\sigma$  associated to the width of this jump. The characterisation of the pristine material leads to  $\sigma/r_m = 0.13$  associated to a certain polydispersity of our material.

Concerning the grafted material it has been characterised by water porosimetry (Figure 2B) of the article). The intrusion pressure, modelled by the Laplace law of capillarity, is expected to vary as the inverse of the pore radius. In presence of polydisperse pores, large pores fills before smaller ones. A point within the intrusion plateau is characterised by a volume  $V$  of intruded water and a liquid pressure  $p$  such that

$$\begin{aligned} V(p) &= \lambda_w L \int_{\infty}^r (r - t_g)^2 e^{-\left(\frac{r-r_g}{\sqrt{2}\sigma}\right)^2} dr \\ &= \lambda_w L \int_{\infty}^{r'(p)} r'^2 e^{-\left(\frac{r'-r_g}{\sqrt{2}\sigma}\right)^2} dr' \end{aligned} \quad (2)$$

with  $t_g$  the average thickness of the grafting agent muffle,  $r_g$  the average pore radius of the grafted material,  $r'(p) = -2\gamma_{lv} \cos \theta / p$  (with  $\gamma_{lv}$  the water surface tension and  $\theta$  the contact angle) and  $\lambda_w L = V_w / \int r' \exp(-(r - r_g)/(\sqrt{2}\sigma)) dr'$  (with  $V_w$  the total intruded volume). The thickness  $t_g$  was estimated to be 0.5 nm by Lefevre *et al*<sup>11</sup> for a coverage density of 1.3 nm<sup>-2</sup>. As our coverage density is twice less than the one of Lefevre *et al* we estimate that for our sample  $t_g \sim 0.25$  nm and  $r_g = r_i - t_g \sim 1.5$  nm. As we measured an average intrusion pressure  $p_{int} = 45$  MPa we estimate  $\theta = \arccos(p_{int} r_g / (2\gamma_{lv})) = 117^\circ$ . As expected this value is smaller than the value measured by Lefevre *et al* for similar, fully grafted, material. Assuming this value to be the same in all pores, we expect that

$$r'(p) = \frac{p_{int} r_g}{p} \quad (3)$$

Combining Eq. 2 and 3 the expression of  $V$  according to  $p$  is used to plot the red dashed curve in Figure 2B) of the article. The good agreement between the experimental points and this theoretical curve suggests that the variation of the intrusion pressure during the intrusion process can be interpreted as a signature of the slight polydispersity of the material and reversely this good agreement confirms the estimation of the polydispersity of the material from the sorption isotherm analysis.

## References

- (1) Lamé, G. *Leçon sur la théorie mathématique de l'élasticité des corps solides*; Bachelier: Paris, France, 1852.
- (2) Timoshenko, S.; Goodier, J. *Theory of Elasticity*, 3rd ed.; McGraw-Hill, 1970.
- (3) Gor, G. Y.; Huber, P.; Weissmüller, J. Elastocapillarity in nanopores: Sorption strain from the actions of surface tension and surface stress. *Physical Review Materials* **2018**, *2*, 1–17.
- (4) Kramer, D.; Weissmüller, J. A note on surface stress and surface tension and their interrelation via Shuttleworth's equation and the Lippmann equation. *Surface Science* **2007**, *601*, 3042–3051.
- (5) Gommès, C. J. Adsorption, Capillary Bridge Formation, and Cavitation in SBA-15 Corrugated Mesopores: A Derjaguin-Broekhoff-de Boer Analysis. *Langmuir* **2012**, *28*, 5101–5115.
- (6) Ustinov, E. A.; Do, D. D. Application of a generalized thermodynamic approach to characterize mesoporous materials. *Colloids and Surfaces A: Physicochemical and Engineering Aspects* **2006**, *272*, 68–81.
- (7) di Meglio, J.-M.; Quere, D.; Brochard-Wyart, F. Films mouillants dans les capillaires. *Compte-Rendu de l'Académie des Sciences* **1989**, *309*, 19–24.
- (8) Pellenq, R. J.; Coasne, B.; Denoyel, R. O.; Coussy, O. Simple phenomenological model for phase transitions in confined Geometry. 2. Capillary condensation/evaporation in cylindrical mesopores. *Langmuir* **2009**, *25*, 1393–1402.
- (9) Deroche, I.; Daou, T. J.; Picard, C.; Coasne, B. Reminiscent capillarity in subnanopores. *Nature Communications* **2019**, *10*, 1–10.
- (10) Picard, C.; Gerard, V.; Michel, L.; Xavier, C.; Charlaix, E. Dynamics of heterogeneous wetting in periodic hybrid nanopores. *Journal of Chemical Physics* **2021**, *154*, 1–11.
- (11) Lefevre, B.; Saugey, A.; Barrat, J. L.; Bocquet, L.; Charlaix, E.; Gobin, P. F.; Vigier, G. Intrusion and extrusion of water in hydrophobic mesopores. *Journal of Chemical Physics* **2004**, *120*, 4927–4938.